IEEE Access
Multidisciplinary | Rapid Review | Open Access Journal

Received June 30, 2020, accepted July 29, 2020, date of publication August 5, 2020, date of current version August 17, 2020.

Digital Object Identifier 10.1109/ACCESS.2020.3014305

Deep Learning for Landslide Recognition in Satellite Architecture

TRONG-AN BUI[1], (Graduate Student Member, IEEE), PEI-JUN LEE[1], (Senior Member, IEEE), KAI-YEW LUM[1], (Member, IEEE), CLARISSA LOH[2], AND KYO TAN[2]

[1]Electrical Engineering Department, National Chi Nan University, Puli 54561, Taiwan
[2]School of Engineering, Nanyang Polytechnic University, Singapore 569830

Corresponding authors: Trong-An Bui (trongan93@gmail.com) and Pei-Jun Lee (pjlee@ncnu.edu.tw)

This work was supported in part by the Ministry of Science and Technology of Taiwan under Contract MOST 107-2221-E-260-017-MY3 and Contract MOST 107-2218-E-006-045.

ABSTRACT Using the optical camera in remote sensing is limited in various environmental conditions. This paper presents a system of combining deep learning and image transform algorithms to detect landslide location in satellite images. In the deep learning part, a convolution neural network is used to classify satellite images contain landslides. From landslide images classified, in order to accurately identify landslides under different lighting conditions, this paper proposes a transformation algorithm Hue – Bi-dimensional empirical mode decomposition (H-BEMD) to determine the landslide region and size. After the location of landslide is detected, we discover the size change of the landslide based on different time points. In this study, we record an accuracy of up to 96% in the classification process, and the accuracy of landslide location almost absolute.

INDEX TERMS H-BEMD, CNN, object recognition, landslide localization, Earth, remote sensing, satellite image.

I. INTRODUCTION

In recent years, satellite technology and remote sensing technology [1] is fast developing. Thus, a large number of works related to image processing in remote sensing of the Earth. Application of satellite remote sensing to capture the Earth is rapidly increasing in number as well as image quality. It plays a significant role in the Earth's surface monitoring. Objects detection in remote sensing [2] is to define one or more objects belong to a class and their locations in the image. Their objects have many different sizes and are divided into two types (small and large). Small objects may be vehicles, ships, planes, buildings, etc. Identifying these small objects helps to monitor urban areas, airports, seaports, etc. To detect smaller objects, higher image resolution of the image is required. Besides, large objects may be forest-covered regions, lakes, river flow, landslides, etc. Environment observation research is also essential in the exploitation of satellite image data. In study of environment, because identifiable objects are in the large size group, we can use medium or low-resolution images to observe an object.

The associate editor coordinating the review of this manuscript and approving it for publication was Frederico Guimarães.

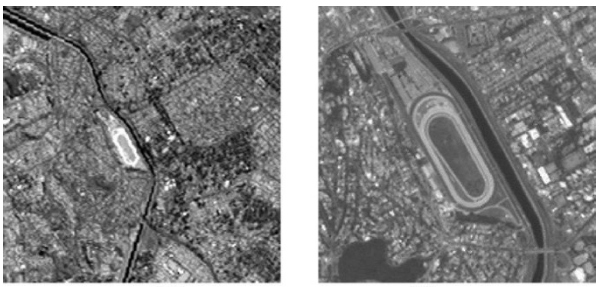

FIGURE 1. Image obtained from the sensor with different spatial resolutions [2]. (a) Landsat-TM, resolution 30m. (b) Alos-AVNIR, resolution 10m.

Figure 1 shows two remote sensing images. Figure 1 (a) is a Landsat-8 [3] image at 30m/pixel resolution, while Figure 1 (b) is an Alos [4] image at 10m/pixel. High-resolution satellite imagery tracks the changing of small objects. Resolution is the first important factor in the exploitation of satellite image data. The second is the revisit time of a (single) satellite, which is the time elapsed between two successive observations on the Earth's surface [5].

The new commercial satellite, also known as super-spectral, may provide the capability to identify materials, e.g., uranium ore (vice copper or iron ore) at a suspect ore

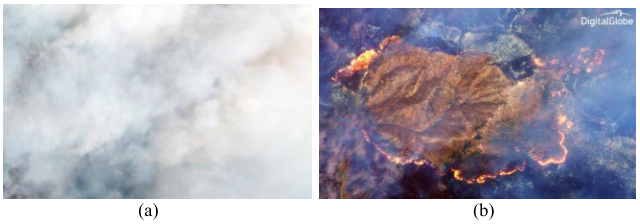

FIGURE 2. Forest fire burning [6]. (a) The visible part of the spectrum – the smoke completely obscures the ground. (b) SWIR image, which made from three of eight SWIR bands – the smoke disappeared and coincidentally give an orange color to the fires.

processing facility. It is also possible to see through thick haze and smoke – Figure 2 [6]. Thus, the third important factor in object detection from satellite image is the multi-spectral data.

Object detection on satellite imagery is kept developing, which many challenges on different objects target. To monitor desertification, a mean of supervised classification and change detection method is introduced [7] that is the optimization of feature extraction and deep learning layer. Deep learning is not only widely applied on satellite optical images, research of mini-UAVs classification [8] introduced architecture to apply CNN in radar. Optimization of deep learning by reducing features in CNN [9] to predict wireless channel parameters of an area directly from a satellite image of the area. Space technology in general and satellite, in particular, are being researched and developed rapidly. Deep learning algorithms are making progress in terms of accuracy, as well as performance [10]. The combination of deep learning and space technology is and will bring expected results.

The Earth is facing global warming and climate change [11]. Therefore, natural disasters occur at an increasing. Earthquakes, tsunamis, storms, floods, and mountain landslides are in high numbers and pose danger to people. Making accurate predictions about natural disasters will help reduce damages to people and property. A landslide is the movement of a mass of rock, debris, or earth down a slope. Landslide are categorized into five models: falls, topples, slides, spreads, and flows. Earthquakes are detected via a seismograph or seismometer. Tsunamis are determined through devices that calculate oscillate in the seabed. Storms and floods are identified and predicted through the combination of wind and precipitation calculation sensors, and satellite imagery. However, landslide areas can be identified and predicted only by satellite images. Landslides have different sizes; from a few hundred meters to several kilometers. Therefore, identifying landslides accurately and predicting their influence plays a vital role in prevention against natural disasters.

Landslide object has a size bigger than other typically objects. Landslides often appear in mountainous and complex terrains. And satellite images are captured landslide areas have a high cloud cover. Therefore, selecting satellite images with a high revisit rate to take advantage of the full amount of data in bulk to conduct analysis. Landsat is a USGS-NASA [3] program that provides us the opportunity to collect valuable resource data. The primary Landsat mission is imaging the Earth. The Landsat database provides free purchase for research purposes with a 30m / pixel image resolution. Besides, Landsat 8 satellite has a 16-day repeat cycle. Finally, Landsat 8 provides multi-spectral bands. R, G, B image channels are easy to collect from multi-spectral bands. Therefore, this paper uses Landsat data to build a landslide dataset in deep learning training and classification. Landsat images also are used to locate landslide and predict direction.

The Global Landslide Catalog (GLC) [12], [13] contains more than 11500 reports on landslides, debris flows, rock avalanches around the world. Based on their size and impact, the GLC divides landslide events into case studies for the classification of landslides. We have five cases of landslide size classification as in Table 1.

TABLE 1. Landslide estimated size [14].

Size	Descriptors	Volumes
Small	Small landslide affecting one hillslope or small area. One road is blocked, cleaned in a few hours; one dump truck needed to clear the dirt, usually no fatalities.	<10 cubic meters
Medium	Moderately sized landslide that could be either a single event or multiple landslides within an area, and involves a large amount of material. Road is blocked for multiple days; multiple roads blocked; multiple houses damaged; multiple dump trucks needed to clear the dirt; sometimes at least one fatality	10 to <1000 cubic meters
Large	Large landslide or series of landslides that occur in one general area but cover a wide area. Substantial impacts to infrastructure and roads, likely moderate to high number of fatalities. Tens to hundreds of people displaced.	1000 to <100,000 cubic meters
Very Large	Very large landslide or multiple events that affect an entire region (often encompassing an entire village). Thousands of people may be displaced, may be high numbers of fatalities.	100,000 to <1 million cubic meters
Catastrophic	Catastrophic impacts to infrastructure and roads. Multiple villages, neighborhoods, towns buried. Tens of thousands of people may be displaced. May be hundreds to thousands of fatalities.	≥1 million cubic meters

Studies image processing on remote sensing use RGB or multi-spectral images (also known as optical images) to identify objects on the Earth's surface. Most approaches uses segmentation and feature detection algorithm [15]–[17]. Object-oriented image analysis – a genetic algorithm – case-based reasoning (OOIA-GA-CBR) [18] is a high – performance classification method for detecting landslides. It consists of three main phases: (1) image processing and multi-image segmentation, (2) feature optimizations, and (3) detecting landslides. A landslide event creates a sloping area of land, which is a soil-covered area. This area has a different color to the surrounding areas (the area in red-region in Figure 3).

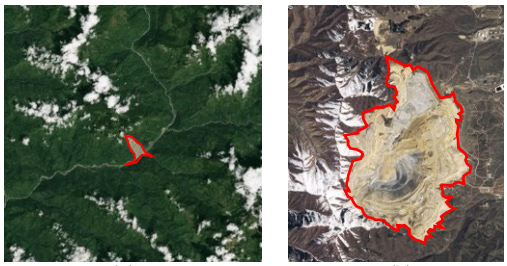

(a) (b)

FIGURE 3. Landslide soil-covered area. (a) A landslide in Nepal. (b) A landslide in Kure, Japan.

When a satellite captures images, environmental factors significantly are affected. Lighting and weather conditions are different, so its have different clarity. Figure 4 shows two land images captured by Landsat 8 using the same camera sensor. With different cloud cover and sunlight ratio, these two images are different in quality. The quality of Figure 4 (a) is better than (b). One of the biggest problems to overcome at pixel level is existence of brightness variation. Hue value in HSV color space is a stable value. Therefore, hue values are more robust towards external lighting changes than RGB color space.

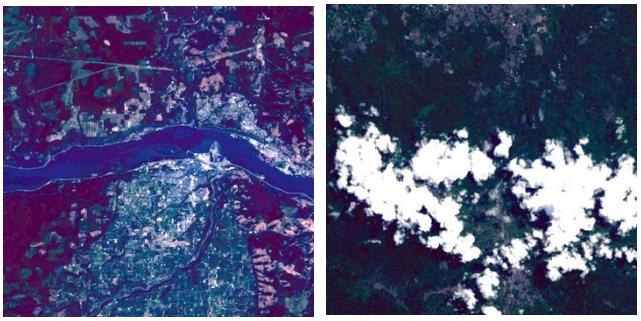

(a) (b)

FIGURE 4. Landsat 8 image with different weather and lighting condition. (a) Free cloud – cloud cover 0% (b) Cloud cover over than 50%.

In pattern recognition, image decomposition plays an important role. The transformation algorithm transforms an image from the spatial domain into the frequency domain. The empirical mode decomposition (EMD) [19] algorithm is an adaptive decomposition method. EMD decomposes a given signal from spatial into frequency components – intrinsic mode functions (IMFs) – by means of an algorithm called sifting process [20]. The bi-dimensional empirical mode decomposition (BEMD) [20] method is a 2D version of the original empirical mode decomposition (EMD). BEMD is an adaptive decomposition method that has been applied widely in the analysis of nonlinear and nonstable signal. BEMD can be adapted for the analysis of nonlinear and non-stationary datasets [21]. Thus, BEMD can adaptively decomposes an image according to the image characteristics, thus extract features at multiple scales or spatial frequencies. 2D IMFs are defined through a 2D sifting process [20] as flow:

- Identify the extrema (both maxima and minima) of the image I by morphological reconstruction [22] based on geodesic operators;
- Generate the 2D 'envelope' by connecting maxima points (respectively, minima points) with a RBF [23];
- Determine the local mean m_1, by averaging the two envelopes;
- Since IMF should have zero local mean, subtract the mean from the image: $I - m_1 = h_1$;
- repeat as h_1 is an IMF.

This study focused on predicting landslide scaling based on remote sensing images. The data collected from satellites play an essential role in this prediction. Based on the Landsat data volume combined with the influence and danger from the size of landslide on table 1, we choose the size of the landslide from medium to catastrophic to build landslide dataset. To solve the effect of light conditions on object recognition, this paper proposes a H-BEMD method to detect the object of interest (soil-covered region) on Earth's surface [24]. However, satellite image come in large quantities, large sizes, and an abundance of different image categories and qualities. Therefore, a deep learning algorithm is used to classify satellite images with or without landslide region. This paper proposes an architecture that combines the advantage of CNN and H-BEMD to detect the landslide region and to predict the scaling of landslide. This paper proposes an architecture that combines deep learning and image processing to detect landslides from satellite image, including:

- landslide dataset from the medium-resolution satellite image;
- landslide region classification by deep learning model (Convolution Neural Network);
- landslide region localization by proposed algorithm with named H-BEMD (Hue Bi-dimensional empirical mode decomposition);
- combined architecture between Convolution Neural Network and H-BEMD.

This paper is organized into four main part:

- Introduction
- Hue – Bi-dimensional empirical mode decomposition (H-BEMD): In this section, we propose an improvement algorithm to detect landslide region on hue channel from satellite image.
- The combination methodology between CNN and H-BEMD: An architecture of combining CNN and Hue-BEMD to predict the scaling of landslide based on satellite image data.
- Simulation Results

II. HUE – BI-DIMENSIONAL EMPIRICAL MODE DECOMPOSITION (H-BEMD)

Equation 1 [25] shows the RGB to HSV color space transformation. With $R, G, B \in [0, 1]$ and $MAX := max(R, G, B)$;

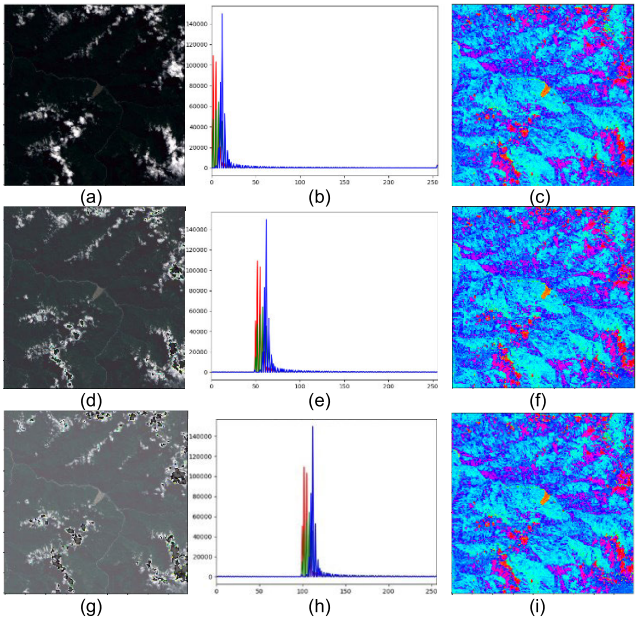

FIGURE 5. Hue channel from satellite image. (a)(d)(c) RGB image with difference lighting condition. (b)(e)(h) Histogram chart of image (a), (d), (c), respective. (c)(f)(i) Hue image of (a), (d), (c), respective.

$MIN = min\,(R, G, B)$, HSV is denoted as:

$$H: \begin{cases} 0, & if\ R = G = B \\ 60° * \left(0 + \dfrac{G - B}{MAX - MIN}\right), & if\ MAX = R \\ 60° * \left(2 + \dfrac{B - R}{MAX - MIN}\right), & if\ MAX = G \\ 60° * \left(4 + \dfrac{R - G}{MAX - MIN}\right), & if\ MAX = B \end{cases} \quad (1.a)$$

$$S: \begin{cases} 0, & if\ R = G = B \\ \dfrac{MAX - MIN}{MAX}, & else; \end{cases} \quad (1.b)$$

$$V := MAX \quad (1.c)$$

HSV separates to luminance from chrominance also known as image intensity. Satellite image is governed by weather, especially the lighting conditions for each shot are different. Figure 5 (a), (d), (g) are RGB satellite images of the same location under different lighting conditions. Figure 5 (b), (e), (h) are the histogram chart of Figure 5 (a), (d), (g), respective. Although the histogram values between 3 images are different, the hue channels– Figure 5 (c)(f)(i) – are the same. Therefore, the hue image channel is selected to detect landslide objects in satellite image.

This paper proposes an algorithm Hue – Bi-dimensional empirical mode decomposition (H-BEMD) to detect landslide objects in satellite images. Figure 6 is the flowchart of the proposed algorithm.

We separate ''Hue – Bi-dimensional empirical mode decomposition (H-BEMD)'' part into two sections. The first section presents the rationale of using sine and cosine of hue values in our process. The second section presents the detailed H-BEMD algorithm.

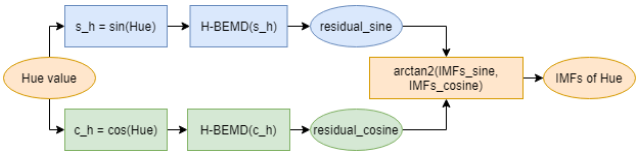

FIGURE 6. H-BEMD flowchart.

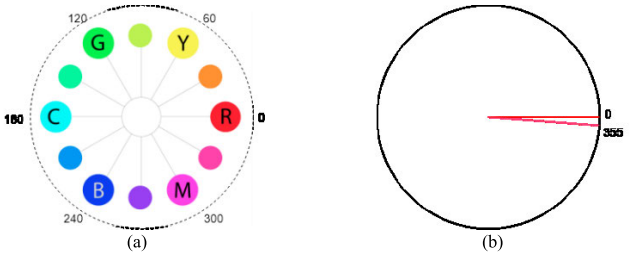

FIGURE 7. Hue channel value presentation.

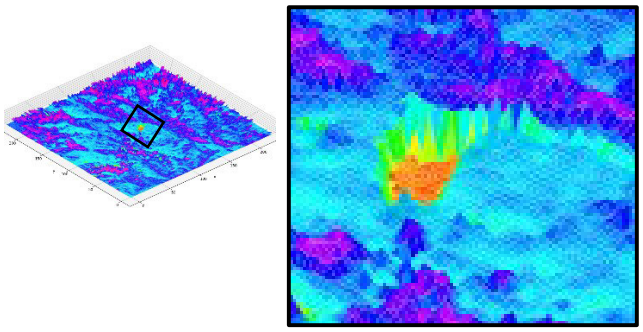

FIGURE 8. Hue channel in satellite image.

A. THE ROLE OF SINE AND COSINE OF HUE

Hue is commonly represented as an angular value from 0 to 360 degrees (or 0 to 2π) – Figure 7. Figure 8 presents the depth hue value of Figure 5 (c).

Figure 8 (a) is a satellite image in hue value, and Figure 8 (b) is the detail of black square region in Figure 8 (a). The region with red-orange and yellow color is a landslide area. However, the red-orange region corresponds to a minimal value of hue, and the yellow corresponds to a maximal value of hue image. This is the region that separates the landslide into two different regions.

To determine the exact maxima and minima, we rely on the maxima and minima values of hue's cosine and sine value. Then, H-BEMD is proposed to do the transformation from sine and cosine values of the hue channel for satellite image. After that, we use the arctan2 of sine and cosine value to get residual hue value – as shown in the flowchart in Figure 6.

B. H-BEMD

This section presents the details of our proposed algorithm (H-BEMD) to detect the landslide region. The $sin(hue)$

and *cos*(*hue*) values are denoted by θ and φ, respectively. H-BEMD adaptively decomposes sine and cosine of hue image (θ and φ) through H-BEMD sifting process as flow:

- Step 1: Detect the extrema (both maxima and minima) points of θ by morphological algorithm, as presented in section 2.2.1.
- Step 2: Connect the maxima and minima points of θ, respectively with a Radial Basis Functions (RBFs) [23] to generate the new 2D 'envelop'.
- Step 3: Normalize the 2D 'envelop' as presented in section 2.2.2.
- Step 3: Determine the local mean m_θ, by averaging the two envelopes.
- Step 4: Subtract out the mean from the image: $\vartheta_i = \theta - m_\theta$;
- Step 5: Follow step 1 to 4 on φ, $\omega_i = \varphi - m_\varphi$
- Step 6: repeat the sifting process with $\theta = \vartheta_i$ and $\varphi = \omega_i$ and $i := i + 1$

The IMF value is the ϑ_i and ω_i with $i = [1, n]$, where n is the number of times the sifting loop is performed. In H-BEMD sifting process, identifying the extrema and normalizing the 2D 'envelop' are two essential part that determine the accuracy and performance of H-BEMD. We present two important parts into two sub-section.

1) EXTREMA POINTS DETECTION BY MORPHOLOGICAL ALGORITHM ON SINE AND COSINE VALUE OF HUE (θ AND φ)

BEMD uses morphological reconstruction by dilation [26] based on geodesic operators to detect image extrema. Hue values have range in [0,360]. Opposite, θ and φ have value range in [−1,1]. Therefore, a new morphological reconstruction algorithm is proposed in this section to detect the maxima and minima points on θ and φ.

Equation 2 represents a dilation of size N.

$$\delta^{(N)} I \widehat{=} \forall p : D \cdot \forall q : N_G(p) \cdot (I[q]) \leftarrow \max(I[p], I[q])) \tag{2}$$

where I is the image, p, and q are pixels, D represents the image domain, and N_G is the pixel neighborhood addressed in the dilation.

$$\delta_C^{(N)} I \widehat{=} \delta^{(1)} I \wedge C, \ldots, N \text{ times} \tag{3}$$

Equation 3 represents geodesic by dilation of size N, where I is the marker, C is the mask and $\wedge$ is the point-wise minimum operator. Reconstruction by dilation is defined as the geodesic dilation operator, $\delta_C^{(1)}$ applied iteratively until stability [26].

Because the characteristic of hue value is a 360-degree closed circle (Figure 7), we propose a process of finding the extrema of separation sine and cosine of Hue value, as shown in Figure 9.

The value range of the input image change from [0, 360] to [−1,1]. Reconstruction by dilation is defined as:

$$\delta_C^{(1)} I \widehat{=} \delta^{(1)} I \wedge C \tag{4}$$

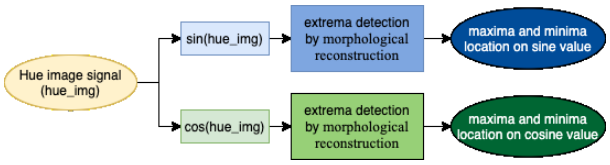

FIGURE 9. Proposal flowchart of extrema detection by morphological reconstruction on Hue value.

where:

- I is θ or φ, respectively.
- C is mask.
- $\wedge$ is the point-wise minimum operator.

Because value domain is changed to [−1,1], so a new mask C is proposed. C is a 2-dimension signal having the same size with I and value of minima degree in range [*sin* (0) , *sin* (360)] and [*cos* (0) , *cos* (360)], as equation [5].

$$C = I - \alpha \tag{5}$$

where α is value of minima point of I.

The coefficient is $\alpha = cos(89°) = sin(1°)$. Because the hue values are stored with radian value in 16 bits, so the α value in 16 bits value is 0.01746. We define the location of maxima and minima points by minus image to reconstruction image as formula [6].

$$\begin{cases} I_{max} = I - \delta_C^{(1)} I \\ I_{min} = (-I) - \delta_C^{(1)}(-I) \\ C = I - \alpha \end{cases} \tag{6}$$

Figure 10 (a) is the maxima (red color) or minima (blue color) regions when applying original extrema detection algorithm from BEMD sifting process [20] on θ or φ. Figure 12 (b) is extrema detection by proposed algorithm at formula [6] on θ or φ.

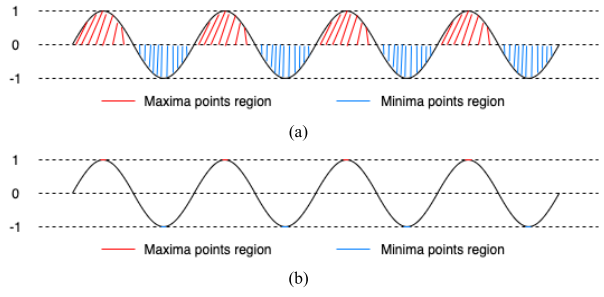

FIGURE 10. The extrema detection on θ or φ. (a) Original Extrema detection on BEMD. (b) Improved Extrema detection on out proposed Hue-BEMD.

To prove the formula for defining extrema location, a hue value image with size 224×224 is applied to identify the maxima and minima points. Figure 11 (a) and (b) are the maxima and minima points detected by the original extrema detection algorithm, respective. This is a 2-dimensional example of Figure 10 (a). In this case, the maxima of 16731 and minima of 44099 points are obtained. Figures 11 (c) and (d) are the maxima and minima points detected by proposed extrema detection formula [6], respectively. This is a 2-dimensional

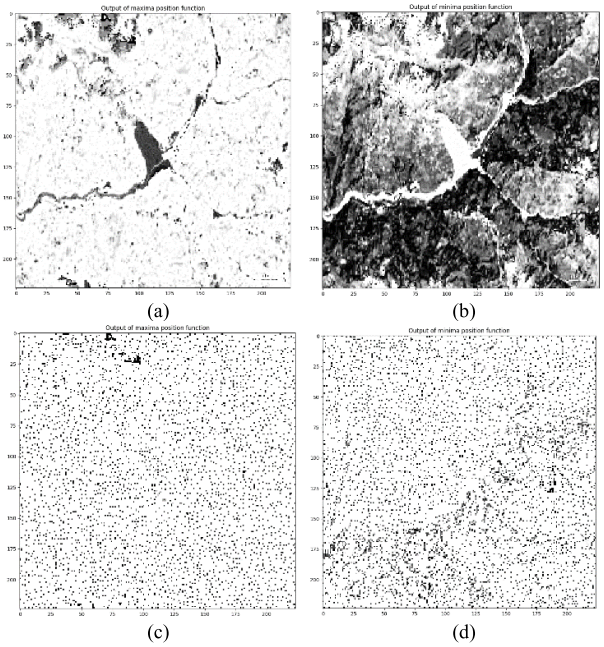

FIGURE 11. Extrema detection from Hue channel. (a) (b) Maxima and minima points detected by original BEMD, respectively. (c) (d) Maxima and minima points detected by Proposal new *J*, respective.

example of Figure 10 (b). We get the maxima of 3867 and minima of 5650 points.

Based on the above results, H-BEMD with new reconstruction function in extreme detection can reduce the number of resources used for the whole algorithm by approximately $((16731/3867 + (44099/5650) \approx 12)$ times.

2) NORMALIZE THE 2D 'ENVELOP'

Figure 12 shows the θ and φ values, respective. The value range is $[-1;1]$. Thus, the maxima value is 1 and minima value is -1. Radial Basis Functions (RBFs) [20] is an algorithm to reconstruct smooth, manifold surfaces from point-cloud data and to repair incomplete meshes. In this sifting process step, a 2D 'envelope' is generated by connecting the maxima points (respectively, minima point) with RBFs. However, RBFs make the value out of range. Therefore, in this section, a normalization function is introduced as well as the role of this function in H-BEMD sifting process. This section is divided into 2 sub sections:

- The first sub-section: we introduce the interpolation and the problems defined.
- The second sub-section: a normalization function is introduced in H-BEMD sifting process as well as this role to make the correctly IMF.

a: INTERPOLATION AND PROBLEMS DEFINED

When first loop of the H-BEMD sifting process ($i = 1$) is done without step 3, we record the result as IMF 1. Figure 13 shows the ϑ_1 value, it is also the θ_2 value.

In Figure 13, the green circles (in Figure 13-a and 13-c) and blue circles (Figure 13-b and 13-c) are the points of maxima and minima value of IMF 1, respectively. The maxima value

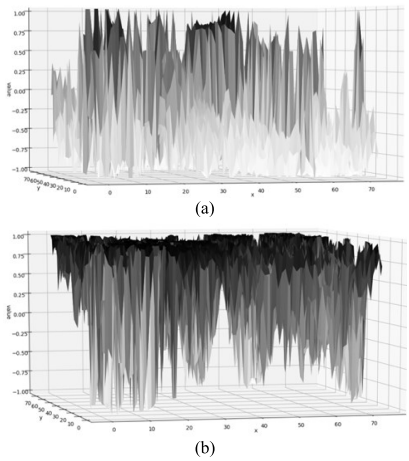

FIGURE 12. Sine and Cosine value. (a) Cosine of Hue. (b) Sine of Hue.

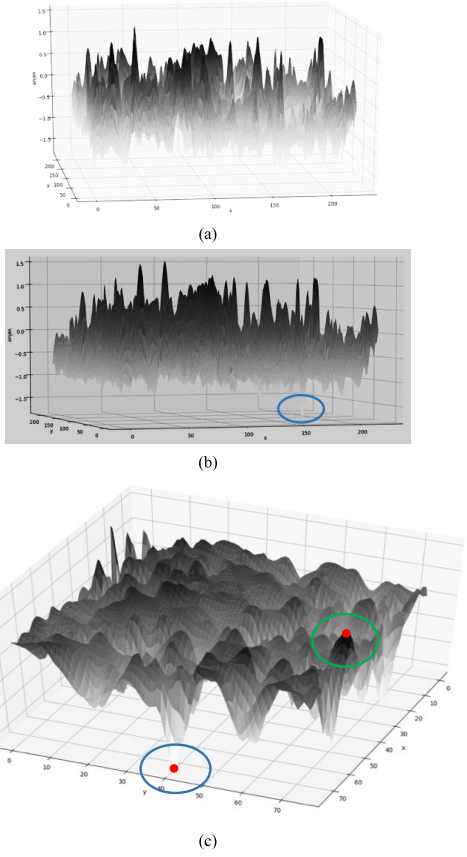

FIGURE 13. IMF 1 with the cosine value of Hue channel.

(green area) record 1.15 and minima value (blue area) is about -1.45. Both maxima and minima points are those created by RBF but exceed the value limit from -1 to 1. This value domain gets bigger after every sifting process. This results in the value range of Hue channel is no longer accurate.

RBF is an algorithm better than cubic spline interpolation [23] of which the primary purpose is interpolating data points on a regular two-dimensional grid. In the first loop of the sifting process, we determine the extrema values.

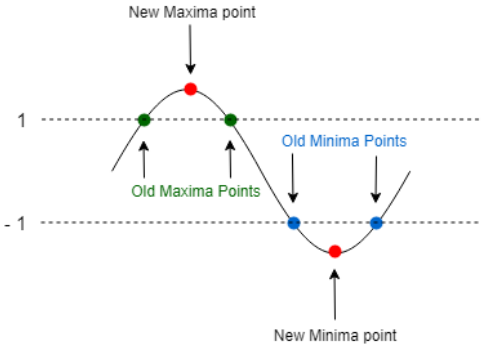

FIGURE 14. RBF problems definition.

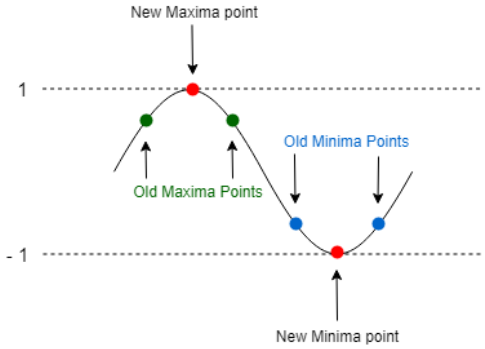

FIGURE 15. Normalized RBF result.

These maxima (or minima) values are adjacent to each other. Suppose we show the maxima and minima detected points in green and blue color, respectively, in Figure 14. RBFs creates a curve (black color) that connects these points. This process creates new maxima and minima points (red color) out of value range. Therefore, in this subsection, our proposed algorithm presents problem-solving to out of value range when connecting the extremals.

b: NORMALIZATION AND ITS ROLE IN H-BEMD SIFTING PROCESS

Normalization is a process that changes the range of pixel intensity values. The motivation is to achieve consistency in the dynamic range for image data.

$$I'_{(x,y)} = \frac{(I_{(x,y)} - a)}{(b - a)} * (\beta - \alpha) + \alpha \tag{7}$$

where $I_{(x,y)}$ and $I'_{(x,y)}$ are original image and normalized image, respectively. b and a are maxima and minima value in $I_{(x,y)}$. β and α are the new upper and lower range boundary in $I'_{(x,y)}$. Figure 15 is the result of the applied formula [7] to the signal in Figure 14. In Figure 14, $\beta, \alpha, b \wedge a$ are upper red-point, lower red-point, green points, and blue points, respective.

Figure 13 (c) is the interpolation result of extrema connection. This process makes the value out of range. Therefore, a normalization function – equation [7] – is applied. Figure 16 shows the result of Figure 13 (c). The green, blue area, and red-point are matching between 2 images. The image value range is changed from $[-1.5;1.5]$ to $[-1;1]$.

Our proposed H-BEMD solves problems missed when applying BEMD on Hue channel to detect landslide region. We present the simulation results recorded during the application of H-BEMD in satellite images as well as adequately address the differences in lighting conditions in the Simulation Results section.

III. THE COMBINATION METHODOLOGY BETWEEN CNN AND H-BEMD

Every day, ground stations receive a large number of satellite images. These images have different shooting times, locations, lighting conditions, and image quality. To classify these images, which images have landslides or do not have landslide, a Convolution Neural Network (CNN) is chosen to conduct image classification. From the classified images, our proposed H-BEMD algorithm is applied to identify landslide location and scaling. Thus, in this section, we present a proposed methodology to combine CNN and H-BEMD to locate the landslide region from satellite database. We divide into two sections:

- In the first section – Convolution Neural Network (CNN) in satellite implementation, we present an architecture and CNN model, which suitable in satellite implementation.
- In the second section – The methodology of combination CNN and BEMD to predict the landslide scaling, we present a method to combine CNN in landslide classification and Hue-BEMD in landslide location. From location labeling, we compare and predict landslide size scaling and direction.

A. CONVOLUTION NEURAL NETWORK (CNN) IN SATELLITE IMPLEMENTATION

Convolution Neural Network (CNN) is a deep learning algorithm. Currently, CNN has many different models, such as VGGNet, ResNet, MobileNet.

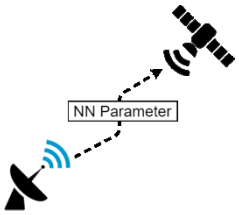

Different from the implementation of conventional CNN applications, the CNN applied model be more careful. Beside satisfies the accurate identification and limitations of satellite hardware, the selection of a CNN has to match with inter-transfer data between satellite and ground stations. Based on inter-send/receive data limits, with CubeSat 3U, the limitation of the upload link is lower than 1Mb/day. Thus, the size of the neural parameters is focused. Besides choosing the lightweight neural network, the computing resource in the inference process is also focused. Floating-point operations per second (FLOPS, flops, or flop/s) is a measure of computer performance, useful in fields of scientific computations that

TABLE 2. Convolution neural network comparison [27].

Architecture	Parameters (MB)	GFLOG-PS	Imagenet Accuracy	
			Top 1	Top 5
AlexNet	237.95	1.132	59.0%	81.8%
VGGNet16	527.79	15.610	74.4 %	91.9 %
ResNet50	102.24	4.140	77.2 %	93.3 %
Inception v3	90.92	5.743	78.9%	94.4%
MobileNet	16.96	0.569	70.7 %	89.5 %
MobileNetv2	**13.5**	**0.360**	**71.7 %**	**91.0 %**

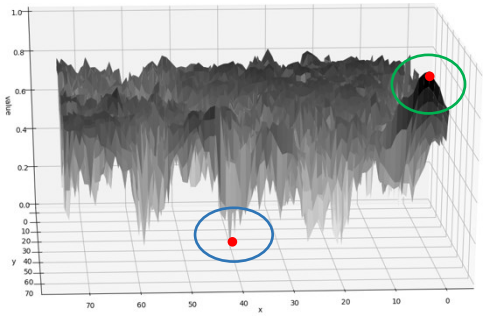

FIGURE 16. Normalized image.

require floating-point calculations. Gigaflops (GFLOPS) is a unit of measurement used to measure the performance of a computer's floating-point unit, commonly referred to as the FPU. One gigaflop is one billion (1,000,000,000) FLOPS.

In our research, we focus on CNN implementation on Cube satellite and small satellites. Therefore, the limitation of hardware and power consumption is focused. Firstly, MobileNetV2 [28] has lowest GFLOGPS. Secondly, the parameters of MobileNetV2, which is the trained data, is the smallest in Table 2. Trained data is uploaded from ground station to satellite when training process is done. It always keeps training when we get more and more satellite image data. Therefore, MobileNetV2 [28] is chosen in the classification deployment with CubeSat 3U.

B. THE METHODOLOGY OF COMBINATION CNN AND BEMD TO PREDICT THE LANDSLIDE SCALING

A combination between CNN and BEMD is presented to classify the landslide region from satellite image. From classification results, we predict the landslide scaling depends on landslide size. Figure 17 is a flowchart of our combination CNN and BEMD methodology to locate landslide region.

In ground station – bellow area with blue square in Figure 17, satellite images collected from Landsat are built to a Landslide dataset. Then, the dataset is used to train with two labels ("*with* landslide" and "without landslide") by MobileNet V2. Adam Optimization [29] is applied to minimize the loss function in training process. The training process finishes with result is network parameters of MobileNet V2.

The network parameters are uploaded from the ground station to satellite. In the satellite process – the top area with

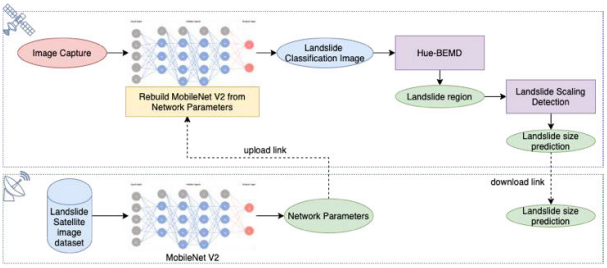

FIGURE 17. BEMD-CNN combination flowchart to predict landslide scaling.

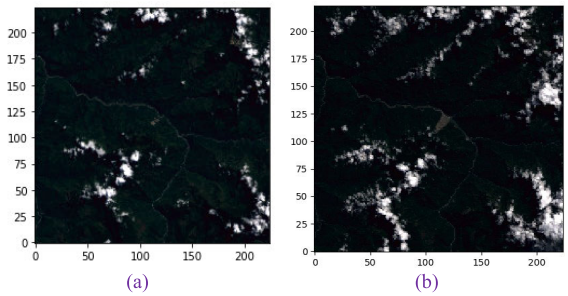

FIGURE 18. Landslide object from satellite image with resolution 10.34m/pixel. (a) Jure landslide [30], [31] in Nepal, captured at September 15, 2013 – time t_1. (b) Jure landslide [30], [31] in Nepal, captured at September 18, 2014 – time t_2.

blue color bounder in Figure 17, MobileNet V2 is rebuilt from parameters. Satellite images are captured by a satellite camera. Figure 18(a) and (b) are satellite images captured at different times. Those images are inputted to neural networks to classify each image that has or does not have landslide regions.

Figure 18 (a) is a landslide region captured from Landsat 8 on September 15, 2013. Figure 18 (b) is a satellite image, which captured by the same sensor with Figure (a) on September 18, 2014. Two images in Figure 18 contain Jure landslide [30]. Figure 18 (a) is captured before landslide event. Opposite, figure 18 (b) is captured after landslide event. Both images have landslide region with a different size. Thus, in our process, MobileNet v2 (rebuild from network parameters) classify two images into label "with landslide" with accuracy value is 0.98 and 0.85, respectively. In this step, the power of CNN is used to classify landslide images.

After that, to locate landslide regions, H-BEMD is applied to classified images. In the study of the application of landslide identification based on H-BEMD, we chose to perform the sifting process twice that mean $n = 2$. The residual values of H-BEMD sifting process are ρ and σ, which are the result of sine and cosine value, respectively.

$$\rho = \theta - \sum_{i=1}^{n} \vartheta_i, \quad n \in N \tag{8.1}$$

$$\sigma = \varphi - \sum_{i=1}^{n} \omega_i, \quad n \in N \tag{8.2}$$

$$\xi_i = arctan2\,(\rho, \sigma)\,, \quad i \in [1, n] \tag{8.3}$$

The residual image ξ_2 is defined by Equation [8.3]. We present the reason to select $n = 2$ based on the actual results and performance of algorithm in Simulation Result

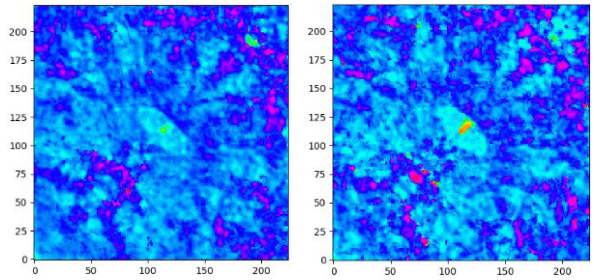

FIGURE 19. Landslide feature – (ξ_2) of Hue-BEMD from Jure Landslide. (a) September 15, 2013. (b) September 18, 2014.

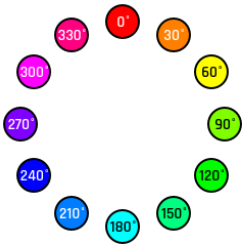

FIGURE 20. Hue value range in Vegetation segmentation.

section. The results of this process (ξ_2 of H-BEMD) are the landslide feature – as shown in Figure 19.

The pixel value on H-BEMD's result is the Hue value, which has value range between 0 to 359. In the next step, landslide regions are identified based on the characteristic color. Hassanein [32] introduces "A New Vegetation Segmentation Approach based on Threshold Detection from Hue value of aerial image".

The achieved results showed its ability to generate accurate and stable vegetation segmentation performance with mean accuracy equal to 87.29% and standard deviation as 12.5%. In this study, landslide regions are identified through soil-covered areas (red-bordering regions in Figure 3). Therefore, based on hue histogram for vegetarian/non-vegetarian [32], we propose to use the threshold value to segmentation landslide regions in range 330° to 90° - as formula [9].

$$-0.5 < \psi < 1 \tag{9}$$

where ψ is the threshold value of ξ_2; -0.5 is value of $sin\,(330°)$, and 1 is value of $sin\,(90°)$.

Figure 21 shows the result of landslide regions localization by thresholding as formula [9]. Finally, landslide scaling and erosion direction are predicted by the regions scaling between Figure 19 (a) and Figure 19 (b). Figure 22 is detailed of red rectangular region in Figure 21.

Image moment is a certain particular weighted average of the image pixel intensities [33], which summarize a shape given image $I(x, y)$ – equation [10].

$$M_{ij} = \sum_x \sum_y x^i y^j I(x, y) \tag{10}$$

where $I(x, y)$ is binary image of the landslide region. In this case, $I(x, y)$ is image in Figure 22(a) or 22(b). A centroid of

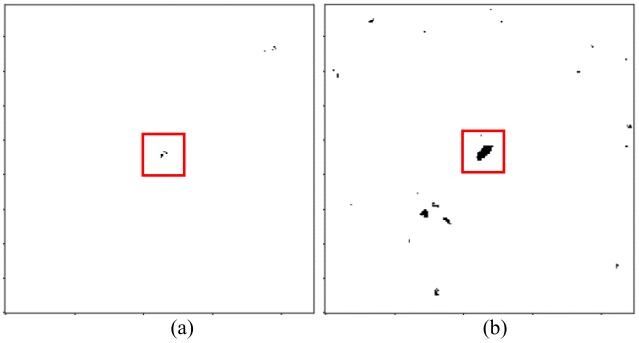

FIGURE 21. Landslide labeling. (a) Labeling of Figure 19-a. (b) Labeling of Figure 19-b.

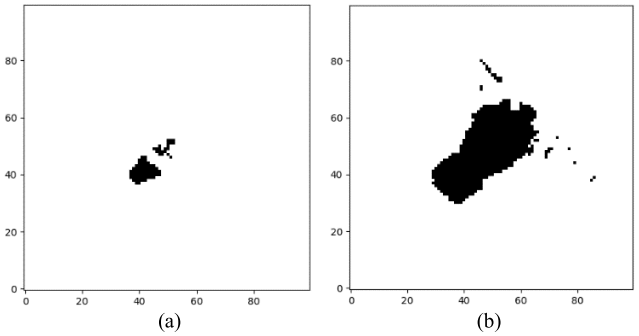

FIGURE 22. Landslide region location.

TABLE 3. Landslide region count points.

	Figure 21 (a)	Figure 21 (b)
Amount of Non-zero point	84	753

landslide shape is $\{\bar{x}, \bar{y}\}$, which is defined as equation [11].

$$\{\bar{x}, \bar{y}\} = \{\frac{M_{10}}{M_{00}}, \frac{M_{01}}{M_{00}}\} \tag{11}$$

The green point (in Figure 23a) and redpoint (in Figure 23b) are centroid points of landslide shape on each case.

Besides, because the landslide image in Figure 22 is a binary image, equation [12] is applied to count non-zero points (N). The non-zero points are the exact landslide region.

$$\mathrm{N}_{I(x,y)} = \sum\nolimits_{I(x,y)\neq 0} 1 \tag{12}$$

where $I\,(x, y)$ is landslide label image – Figure 22.

From results of Table 3, the scaling region (Υ) is defined by equation [13].

$$\Upsilon = (\mathrm{N}_{I'(x,y)} - \mathrm{N}_{I(x,y)}) \times resolution \tag{13}$$

where $\mathrm{N}_{I'(x,y)}$ is the amount of non-zero point of landslide at time t_2 and $\mathrm{N}_{I(x,y)}$ is the amount of non-zero point of landslide at time t_1. In this case, $\mathrm{N}_{I'(x,y)}$ and $\mathrm{N}_{I(x,y)}$ are 753 and 84, respectively. The resolution of this image is

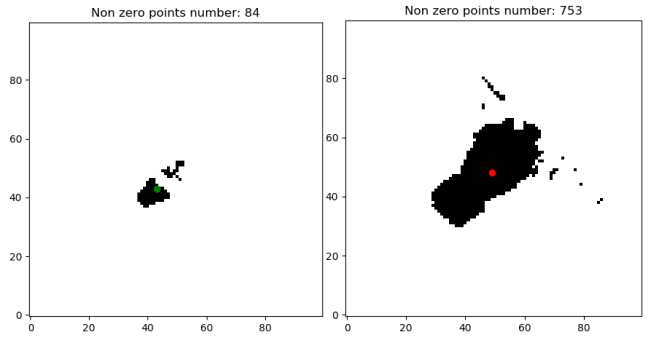

FIGURE 23. The centroid of landslide region.

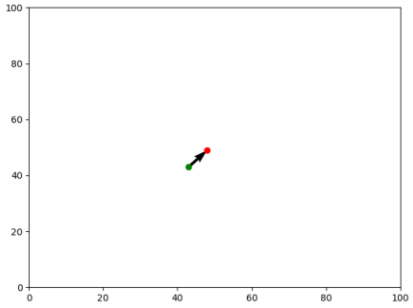

FIGURE 24. Landslide scaling direction.

$30m^2/pixel$. Therefore, the scaling of landslide region is $\Upsilon = (753 - 84) \times 30 = 20070m^2$.

From the centroid point of landslide region in difference time (t_1 *and* t_2), a vector is defined, which is the direction of landslide scaling. Figure 24 is the scaling direction of landslide on Figure 23.

IV. SIMULATION RESULT

In this section, we present the results based on the flowchart of Figure 17. We give each step from the training of the Landslide data set to prediction of the Landslide scaling areas.

A. TRAINING LANDSLIDE DATASET FROM SATELLITE IMAGE

In this paper, satellite images are collected from Landsat 8 via USGS [3]. The satellite has a 16-days repeat cycle. The image resolution is 30m/pixel in multi-spectral. In training process, Adam optimization [29] is applied. Adam is an adaptive learning rate method, which computes individual learning rates for different parameters.

The learning rate configuration in Adam optimization algorithm [29] is $\boldsymbol{\alpha} = \mathbf{0.0001}$. The batch size configuration is **150**. The epochs in training step are **250**. The early stopping is configured by accuracy values are not increased by **20** epoch. Figure 25 is the training result of the training landslide image process. Table 4 is the output of neural network, which is parameters size.

Currently, the dataset is built by Landsat 8 images. The positive data ''with landslide'' is defined by GLC, and the

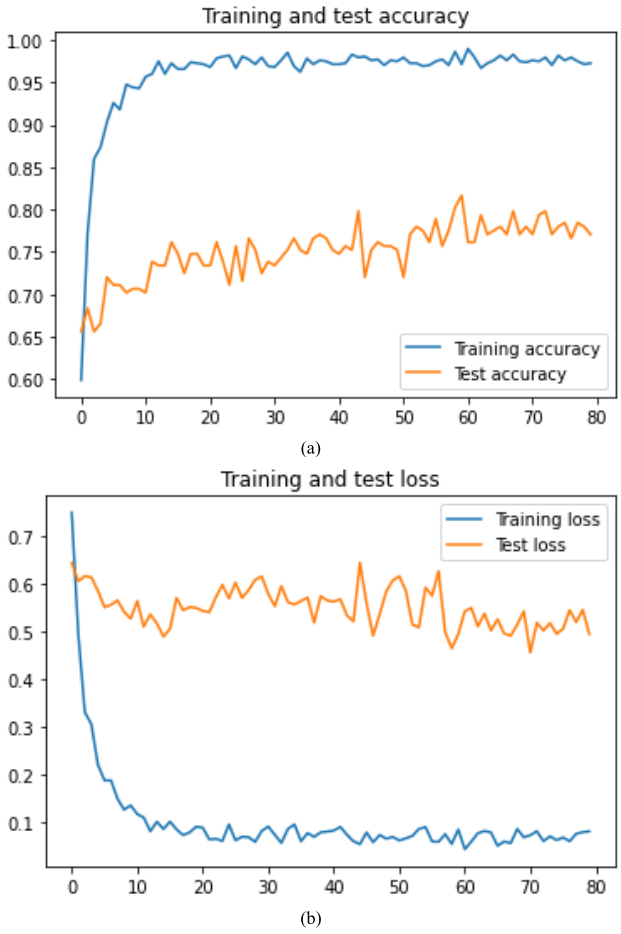

FIGURE 25. Training accuracy and loss value. (a) Training and test accuracy value. (b) Train and test loss value.

TABLE 4. Neural network parameters – training output.

Trainable params	Non-trainable params	Total params
3,871,234	39,232	3,910,466

negative data ''without landslide'' is random by GPS location not in the list of GLC. This dataset is currently very accurate with positive data. However, negative data is incorrect. So the limitations of the data set make a big difference between the two labels during training. Improving this dataset is our goal to complete the study.

B. LANDSLIDE IMAGE CLASSIFICATION

As a result of the training, landslide images are classified from satellite images. In this part, the experiment results are presented based on a sample data set from Landsat 8.

Figure 26 is the result of the classification process for classifying images that do not contain landslide by CNN. All

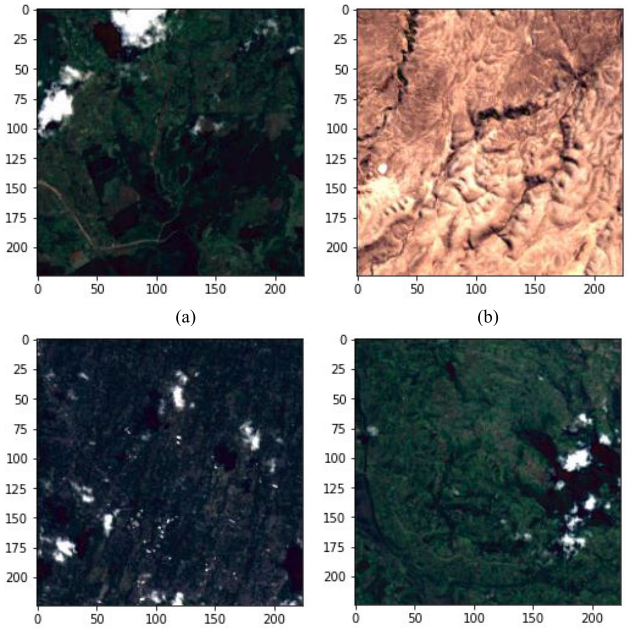

FIGURE 26. Classification results with CNN – label "without landslide".

TABLE 5. Landslide classification accuracy by MobileNet V2.

	"Landslide"	"Without Landslide"
Fig.26 (a)	0.17741571	**0.8225843**
Fig.26 (b)	0.447432	**0.55256796**
Fig.26 (c)	0.008785016	**0.991215**
Fig.26 (d)	0.036235865	**0.96376413**
Fig.27 (a)	**0.70610897**	0.293897
Fig.27 (b)	**0.74854316**	0.25145682
Fig.27 (c)	**0.93308794**	0.066912115
Fig.27 (d)	**0.8898166**	0.1101834
Fig.27 (e)	**0.62268275**	0.37731728
Fig.27 (f)	**0.98423797**	0.015762087

images in Figure 26 have landslide region, and Table 5 is the accuracy of landslide classification in Figure 27.

From this classified results, H-BEMD is used to locate landslide regions in satellite images.

C. LANDSLIDE REGION DETECTION WITH HUE-BEMD

In this section, we present the proposed algorithm results. Also, we compare our algorithm results compared to the original algorithm.

1) LANDSLIDE FEATURE BY ORIGINAL BEMD ON HUE CHANNEL

Figure 28 is $\boldsymbol{\xi_2}$ by original BEMD [20] algorithm. This is simulation result of original BEMD algorithm when apply on Hue channel. With this result, we cannot recognize the location of landslide.

2) LANDSLIDE FEATURE BY PROPOSED HUE-BEMD

Figure 29 is the $\boldsymbol{\xi_2}$ by our proposed algorithm (H-BEMD).

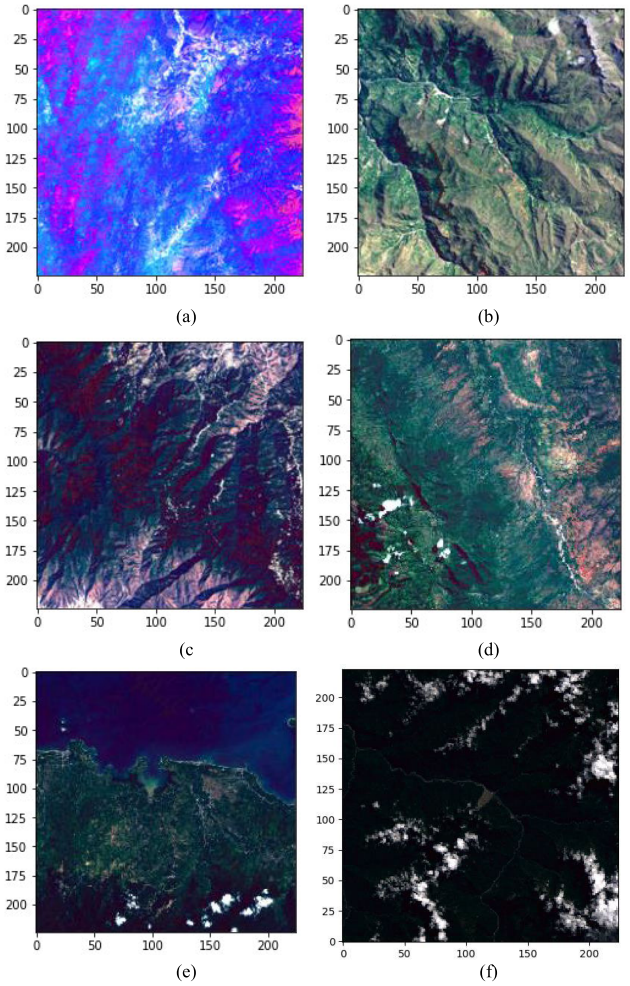

FIGURE 27. Classification results with CNN – label "with landslide".

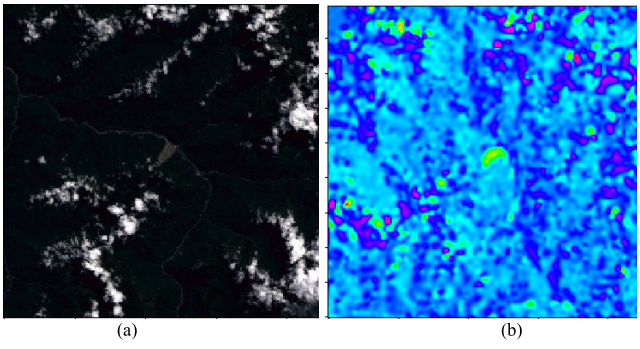

FIGURE 28. The results of original BEMD [20] – IMF 3 of sifting process. (a) Original image. (b) IMF3.

With H-BEMD, we recognize the location of landslide on ξ_1, ξ_2 and ξ_3. Figure 30 shows the details of landslide region in ξ_1, ξ_2 and ξ_3, respectively.

We compare three figures (a), (b), and (c) in Figure 30. Figure (a) still contains much noise - the position has pink color. Figure (b) reduces the amount of noise compared to figure (a). In Figure (c), the size of landslide is reduced compared to Figure (b). Therefore, image (b) with ξ_2 is selected to identify the landslide region in the satellite image.

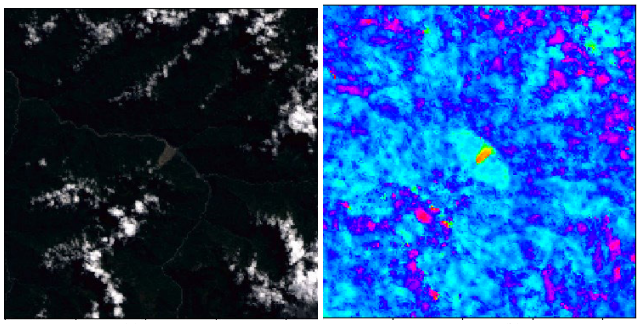

FIGURE 29. The results of proposed Hue – BEMD – IMF 3 of sifting process. (a) Original image. (b) IMF3.

TABLE 6. Performance comparison on sifting process.

	Sifting process loop count	Memory (byte)	CPU execute time (second)
ξ_1	1	52199424	132
ξ_2	2	20279296	52
ξ_3	3	4288512	38

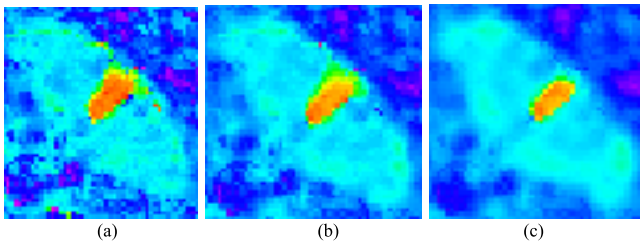

FIGURE 30. Landslide region in residual value of proposed H – BEMD algorithm.

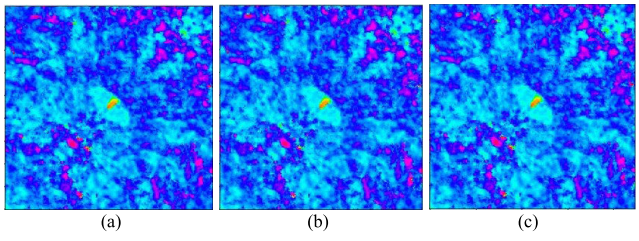

FIGURE 31. Landslide region segmentation from Original Satellite image. (g) landslide feature region (ξ_2) of H-BEMD from Figure 5(a). (h) landslide feature region (ξ_2) of H-BEMD from Figure 5(d). (i) landslide feature region (ξ_2) of H-BEMD from Figure 5(g).

Another essential factor to decide on the selection of the n value, we compare the performance of the sifting process. Table 6 is a performance comparison for determining the ξ. Besides better accuracy, ξ_2 also has average performance value compared to ξ_1 and ξ_3.

When analyzing images from satellites, light conditions greatly influence the identification of objects correctly. Experiment results in identifying the landslide through our proposed algorithm with different lighting conditions is presented at Figure 31.

Figure 5 (a), (d) and (g) are the satellite image with different lighting conditions. Figure 31 (a), (b) and (c) are the

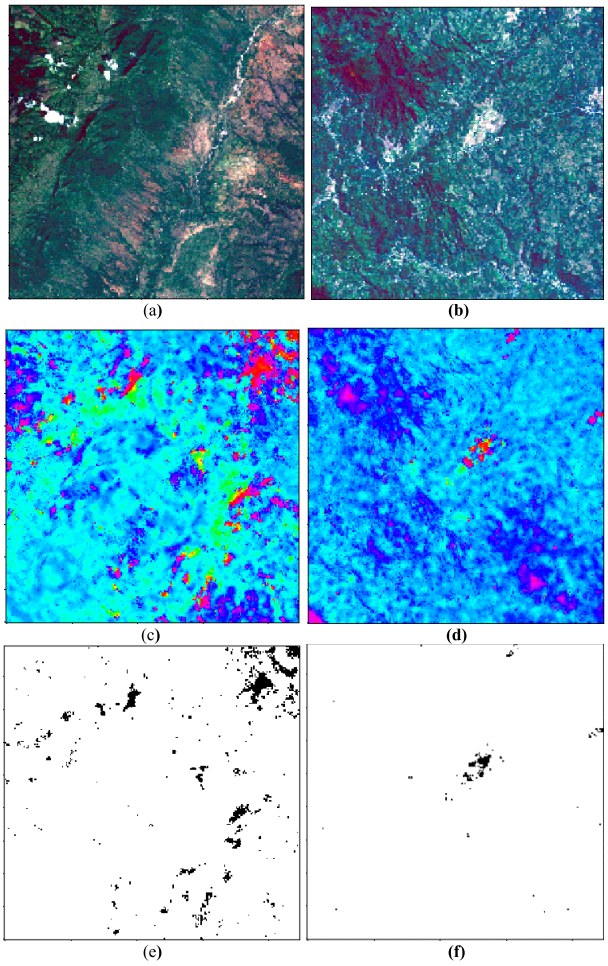

FIGURE 32. Landslide location from the combination of CNN and Hue-BEMD. (a) (b) satellite image with landslide classified. (c) (d) landslide feature region (ξ_2) of (a) and (b), respectively. (e) (f) landslide labeling of (c) and (d), respectively.

landslide feature region (ξ_2) of H-BEMD sifting process. However, these three image results are the same value. Therefore, our proposed algorithm can solve the problem of light and external conditions for landslide detection on satellite images.

D. LANDSLIDE LOCATION FROM SATELLITE IMAGE

In this section, we present additional results to demonstrate the validity of our improvement method and algorithm in this paper.

V. CONCLUSION

We have presented a method for landslide localization from satellite image. Our proposed algorithm has been shown the combination between an image classification through deep learning and adaptive transform algorithm by CNN and H-BEMD. Then, we have presented a method to predict landslide size scaling and direction. Simulation results show satellite images with landslide classified as well as landslide localization. We have presented landslide scaling and

direction prediction on case of Jure landslide with event recorded in 2014.

In this paper, the maxima and minima are determined based on sine and cosine of hue value. Because hue values commonly represented as an angular value, so 360 not really is a maxima value and 0 is not a minima value. We are continuing to work and find a method that improves the extreme method. Current method addresses the impact of different light environmental conditions on images. However, the results are still affected by cloud cover. With a lot of coverage, the process of identifying objects is noisy. While deep learning greatly enhances the capability of landslide localization, we recognize that current satellite hardware may not be adequate to perform such computations on-board or in real time.

This study is an applied research and practical implementation for small satellites (Cube satellite 3U). Therefore, the hardware limitations, as well as the practical implementation of the algorithms, have been our concern. We are continually working to provide accurate identification and real-time detection on satellite.

REFERENCES

[1] J. Li, F. Xing, P. K. Shrestha, F. Shi, and Z. Liu, "On-orbit self-focusing using conjugated optical fiber waveguides for space optical cameras," *IEEE Geosci. Remote Sens. Lett.*, vol. 16, no. 11, pp. 1703–1705, Nov. 2019, doi: 10.1109/LGRS.2019.2909825.

[2] L. M. G. Fonseca, L. M. Namikawa, and E. F. Castejon, "Digital image processing in remote sensing," in *Proc. Tuts. XXII Brazilian Symp. Comput. Graph. Image Process.*, Oct. 2009, pp. 59–71, doi: 10.1109/SIBGRAPI-Tutorials.2009.13.

[3] *Landsat—Earth Observation Satellites (ver. 1.1, Aug. 2016): U.S. Geological Survey Fact Sheet 2015-3081*, U. S. Geological Survey, Reston, VA, USA, 2016, doi: 10.3133/fs20153081.

[4] ASF. (2016). *About ALOS PALSAR*. ASF. Accessed: May 4, 2020. [Online]. Available: https://www.eorc.jaxa.jp/ALOS/en/about/about_index.htm

[5] X. Luo, M. Wang, G. Dai, and X. Chen, "A novel technique to compute the revisit time of satellites and its application in remote sensing satellite optimization design," *Int. J. Aerosp. Eng.*, vol. 2017, pp. 1–9, 2017, doi: 10.1155/2017/6469439.

[6] F. Pabian, "Commercial satellite imagery as an evolving open-source verification technology: Emerging trends and their impact for nuclear nonproliferation analysis," Publications Office Eur. Union, Tech. Rep. EUR27687, 2015. [Online]. Available: https://ec.europa.eu/jrc/en/publication/commercial-satellite-imagery-evolving-open-source-verification-technology-emerging-trends-and-their, doi: 10.2789/933810.

[7] S. A. Azzouzi, A. Vidal-Pantaleoni, and H. A. Bentounes, "Desertification monitoring in biskra, algeria, with landsat imagery by means of supervised classification and change detection methods," *IEEE Access*, vol. 5, pp. 9065–9072, 2017, doi: 10.1109/ACCESS.2017.2700405.

[8] A. Huizing, M. Heiligers, B. Dekker, J. de Wit, L. Cifola, and R. Harmanny, "Deep learning for classification of mini-UAVs using micro-Doppler spectrograms in cognitive radar," *IEEE Aerosp. Electron. Syst. Mag.*, vol. 34, no. 11, pp. 46–56, Nov. 2019, doi: 10.1109/MAES.2019.2933972.

[9] H. F. Ates, S. M. Hashir, T. Baykas, and B. K. Gunturk, "Path loss exponent and shadowing factor prediction from satellite images using deep learning," *IEEE Access*, vol. 7, pp. 101366–101375, Jul. 2019, doi: 10.1109/access.2019.2931072.

[10] P. Valter, P. Lindgren, and R. Prasad, "The consequences of artificial intelligence and deep learning in a world of persuasive business models," *IEEE Aerosp. Electron. Syst. Mag.*, vol. 33, nos. 5–6, pp. 80–88, May 2018, doi: 10.1109/MAES.2018.170110.

[11] *Centre for Research on the Epidemiology of Disasters*, Centre for Research on the Epidemiology of Disasters, Brussels, Belgium, United Nations Off. Diaster Risk Reduct., 2015, p. 37, doi: 10.1017/CBO9781107415324.004.

[12] D. Kirschbaum, T. Stanley, and Y. Zhou, "Spatial and temporal analysis of a global landslide catalog," *Geomorphology*, vol. 249, pp. 4–15, Nov. 2015, doi: 10.1016/j.geomorph.2015.03.016.

[13] D. B. Kirschbaum, R. Adler, Y. Hong, S. Hill, and A. Lerner-Lam, "A global landslide catalog for hazard applications: Method, results, and limitations," *Natural Hazards*, vol. 52, no. 3, pp. 561–575, Mar. 2010, doi: 10.1007/s11069-009-9401-4.

[14] *Landslide Reporter Primer and Landslide Identification The Landslide Reporter's Guide*. Accessed: Feb. 9, 2020. [Online]. Available: https://gpm.nasa.gov/landslides/guides/COOLRGuide_Primer.pdf

[15] M. Moine, A. Puissant, and J.-P. Malet. (2010). *Detection of Landslides From Aerial and Satellite Images With a Semi-Automatic Method. Application to the Barcelonnette Basin (Alpes-de-Hautes-Provence, France)*. Accessed: Feb. 16, 2020. [Online]. Available: https://halshs.archives-ouvertes.fr/halshs-00467545

[16] M. Alvioli, A. C. Mondini, F. Fiorucci, M. Cardinali, and I. Marchesini, "Topography-driven satellite imagery analysis for landslide mapping," *Geomatics, Natural Hazards Risk*, vol. 9, no. 1, pp. 544–567, Jan. 2018, doi: 10.1080/19475705.2018.1458050.

[17] J. Nichol and M. S. Wong, "Satellite remote sensing for detailed landslide inventories using change detection and image fusion," *Int. J. Remote Sens.*, vol. 26, no. 9, pp. 1913–1926, May 2005, doi: 10.1080/01431160512331314047.

[18] J. Dou, K.-T. Chang, S. Chen, A. Yunus, J.-K. Liu, H. Xia, and Z. Zhu, "Automatic case-based reasoning approach for landslide detection: Integration of object-oriented image analysis and a genetic algorithm," *Remote Sens.*, vol. 7, no. 4, pp. 4318–4342, Apr. 2015, doi: 10.3390/rs70404318.

[19] N. E. Huang, Z. Shen, and S. R. Long, "The empirical mode decomposition and the Hilbert spectrum for nonlinear and non-stationary time series analysis," *Proc. Roy. Soc. London. A, Math., Phys. Eng. Sci.*, vol. 454, no. 1971, pp. 903–995, 1998, doi: 10.1098/rspa.1998.0193.

[20] J. C. Nunes, Y. Bouaoune, E. Delechelle, O. Niang, and P. Bunel, "Image analysis by bidimensional empirical mode decomposition," *Image Vis. Comput.*, vol. 21, no. 12, pp. 1019–1026, Nov. 2003, doi: 10.1016/S0262-8856(03)00094-5.

[21] G. Liu, L. Li, H. Gong, Q. Jin, X. Li, R. Song, Y. Chen, Y. Chen, C. He, Y. Huang, and Y. Yao, "Multisource remote sensing imagery fusion scheme based on bidimensional empirical mode decomposition (BEMD) and its application to the extraction of bamboo forest," *Remote Sens.*, vol. 9, no. 1, p. 19, Dec. 2016, doi: 10.3390/rs9010019.

[22] L. Vincent, "Morphological grayscale reconstruction in image analysis: Applications and efficient algorithms," *IEEE Trans. Image Process.*, vol. 2, no. 2, pp. 176–201, Apr. 1993, doi: 10.1109/83.217222.

[23] J. C. Carr, W. R. Fright, and R. K. Beatson, "Surface interpolation with radial basis functions for medical imaging," *IEEE Trans. Med. Imag.*, vol. 16, no. 1, pp. 96–107, 1997, doi: 10.1109/42.552059.

[24] T.-A. Bui, P.-J. Lee, K.-Y. Lum, C.-R. Chen, and S.-H. Shiu, "Using BEMD in CNN to identify landslide in satellite image," in *Proc. Int. Conf. Syst. Sci. Eng. (ICSSE)*, Jul. 2019, pp. 94–97, doi: 10.1109/ICSSE.2019.8823128.

[25] M. Loesdau, S. Chabrier, and A. Gabillon, *Hue and Saturation in the RGB Color Space* (Lecture Notes in Computer Science: Lecture Notes in Artificial Intelligence and Lecture Notes in Bioinformatics), vol. 8509. 2014, pp. 203-212, doi: 10.1007/978-3-319-07998-1_23.

[26] K. Robinson and P. F. Whelan, "Efficient morphological reconstruction: A downhill filter," *Pattern Recognit. Lett.*, vol. 25, no. 15, pp. 1759–1767, Nov. 2004, doi: 10.1016/j.patrec.2004.07.002.

[27] J. Deng, W. Dong, R. Socher, L.-J. Li, K. Li, and L. Fei-Fei, "Imagenet: A large-scale hierarchical image database," in *Proc. IEEE Conf. Comput. Vis. Pattern Recognit.*, Jun. 2009, pp. 248–255, doi: 10.1109/CVPR.2009.5206848.

[28] M. Sandler, A. Howard, M. Zhu, A. Zhmoginov, and L.-C. Chen, "MobileNetV2: Inverted residuals and linear bottlenecks," in *Proc. IEEE/CVF Conf. Comput. Vis. Pattern Recognit.*, Jun. 2018, pp. 4510–4520, doi: 10.1109/CVPR.2018.00474.

[29] D. P. Kingma and J. L. Ba, "Adam: A method for stochastic optimization," Dec. 2015, *arXiv:1412.6980*. Accessed: Aug. 5, 2020. [Online]. Available: https://arxiv.org/abs/1412.6980v9

[30] NASA Earth Observatory. (2014). *Before and After the Sunkosi Landslide*. Luton News. Accessed: Apr. 23, 2020. [Online]. Available: https://earthobservatory.nasa.gov/images/84406/before-and-after-the-sunkosi-landslide

[31] *Sunkoshi landslide | IPLHQ*. Accessed: May 19, 2020. [Online]. Available: https://iplhq.org/report/sunkoshi-landslide/
[32] M. Hassanein, Z. Lari, and N. El-Sheimy, "A new vegetation segmentation approach for cropped fields based on threshold detection from hue histograms," *Sensors*, vol. 18, no. 4, p. 1253, Apr. 2018, doi: 10.3390/s18041253.
[33] M.-K. Hu, "Visual pattern recognition by moment invariants," *IEEE Trans. Inf. Theory*, vol. 8, no. 2, pp. 179–187, Feb. 1962, doi: 10.1109/TIT.1962.1057692.

TRONG-AN BUI (Graduate Student Member, IEEE) received the B.Sc. degree from the Faculty of Information Technology, Ho Chi Minh University of Education, Vietnam, in 2015, and the M.S. degree in image processing from National Chi Nan University, Taiwan, in 2018, where he is currently pursuing the Ph.D. degree. His current research interests include neural networks and artificial intelligence, computer vision and image processing, video coding and data compression, and satellite.

PEI-JUN LEE (Senior Member, IEEE) received the Ph.D. degree from the Department of Electrical Engineering, National Taiwan University, in 2004. Since August 2015, she has been a Distinguished Professor with the Department of Electrical Engineering, National Chi Nan University, Taiwan. Her research interests include 2D/3D image conversion, 3D/multi-view video coding, video communication, video compression, image processing, robot fish, and FPGA system application. She was a recipient of the First Runner-Up and the Outstanding Advisor of the Macronix Golden Silicon Awards Semiconductor Design and Application Competition from MXIC Company Ltd, in 2008.

KAI-YEW LUM (Member, IEEE) received the Diplôme d'Ingénieur degree from the Ecole Nationale Supérieure d'Ingénieurs Electriciens de Grenoble, Grenoble, France, in 1988, and the M.Sc. and Ph.D. degrees from the Department of Aerospace Engineering, University of Michigan, Ann Arbor, in 1995 and 1997, respectively. He was a Technical Staff Member in control and guidance with the DSO National Laboratories, Singapore, from 1998 to 2001. From 2001 to 2011, he was with the Temasek Laboratories, National University of Singapore, Singapore, as a Principal Investigator in control, guidance, and multiagent systems. In 2011, he joined National Chi Nan University, Nantou, Taiwan, where he is currently a Professor of electrical engineering. His current research interests include nonlinear dynamics and control, navigation, sensor networks, and systems identification. He is a member of the American Institute of Aeronautics and Astronautics.

CLARISSA LOH received the B.Sc. degree from Nanyang Polytechnic University, Singapore.

KYO TAN received the B.Sc. degree from Nanyang Polytechnic University, Singapore.